

Microstructure and properties of nano-laminated $Y_3Si_2C_2$ ceramics fabricated via *in situ* reaction by spark plasma sintering

Lin-Kun Shi

Kunming University of Science and Technology

Xiaobing Zhou (✉ zhouxb@nimte.ac.cn)

Ningbo Institute of Materials Technology and Engineering, Chinese Academy of Sciences

<https://orcid.org/0000-0001-8258-3729>

Jian-Qing Dai

Kunming University of Science and Technology

Ke Chen

Ningbo Institute of Materials Technology and Engineering CAS

Zhengren Huang

Ningbo Institute of Materials Technology and Engineering CAS

Qing Huang

Ningbo Institute of Materials Technology and Engineering CAS

Research Article

Keywords: $Y_3Si_2C_2$, Rare earth silicide carbides, Spark plasma sintering, Ternary layered structure ceramic, Property

Posted Date: October 8th, 2020

DOI: <https://doi.org/10.21203/rs.3.rs-86504/v1>

License:  This work is licensed under a Creative Commons Attribution 4.0 International License.

[Read Full License](#)

Abstract

A new nano-laminated $Y_3Si_2C_2$ ceramic material, for the first time, was successfully synthesized via *in situ* reaction between YH_2 and SiC by spark plasma sintering. A MAX phase-like ternary layered structure of $Y_3Si_2C_2$ was observed at the atomic-scale by high resolution transmission electron microscopy. The lattice parameters calculated from both X-ray diffraction and selected area electron diffraction patterns are in good agreement with the reported theoretical results. The nano-laminated fracture of kink boundaries, delamination, and slipping was observed at the tip of the Vickers indent. The values of elastic modulus and Vickers hardness of the $Y_3Si_2C_2$ ceramics sintered at 1500 °C were 156 and 6.4 GPa, respectively. The corresponding values of thermal and electrical conductivity were $13.7 \text{ W m}^{-1} \text{ K}^{-1}$ and $6.3 \times 10^5 \text{ S m}^{-1}$, respectively.

1. Introduction

Rare earth silicide carbides ($RE_3Si_2C_2$, RE = Y, La-Nd, Sm, Gd-Tm) belong to a new group of ternary layered structure materials, which were first developed by Gerdes et al. in 1998 [1, 2]. The crystal structure of these compounds shows an orthorhombic subcell and consists of at least two different superstructures [2]. All the $RE_3Si_2C_2$ compounds were reported to have metallic conductivity and their magnetic ordering temperatures are lower than 60 K [1]. $Y_3Si_2C_2$ is one of a typical representative member of the $RE_3Si_2C_2$ group. In the $Y_3Si_2C_2$ structure, the *c* axis of the subcell is doubled, thus it crystallizes in the body-centered orthorhombic system with space group *Imma* (No. 74) [3]. On the other hand, in $Y_3Si_2C_2$ structure, Y atoms form two-dimensionally arranged infinite sheets of edge-sharing octahedra containing C_2 pairs, wherein zig-zag chains of Si atoms are interleaved [2].

Zhou et al. theoretically predicted that the bulk modulus and shear modulus of $Y_3Si_2C_2$ are 93 and 50 GPa, respectively [3]. Moreover, it was concluded that it is a soft ceramic material with good damage tolerance, due to the low shear deformation resistance and low Pugh's ratios ($G/B = 0.537$; where G: shear modulus; B: bulk modulus) with low Vickers hardness of 6.9 GPa. Furthermore, the calculated volume expansion upon oxidation of $Y_3Si_2C_2$ was found to be ~ 26%, which could potentially lead to the sealing of the cracks between silicon carbide fibers (SiC_f) and SiC matrix. Therefore, $Y_3Si_2C_2$ may be a promising interphase material for SiC fiber-reinforced SiC matrix (SiC_f/SiC) composite, because of the fascinating combined merits including easy cleavage, low shear deformation resistance, and volume expansions upon oxidation [3].

On the other hand, $Y_3Si_2C_2$ is inert when in contact with SiC at temperature up to 1560 °C, while a liquid phase can be formed at temperatures above 1560 °C via a ternary eutectic reaction, according to the calculated Y–Si–C ternary phase diagram [4]. Thus, $Y_3Si_2C_2$ was successfully used as sintering additive for SiC and/or SiC/Al_4SiC_4 system [5, 6]. The presence of a liquid phase not only effectively promotes the densification of SiC and/or SiC/Al_4SiC_4 , but also improves the fracture toughness of ceramics by

optimizing the grain boundary structure. Most importantly, $Y_3Si_2C_2$ can get decomposed into SiC and Y_2O_3 (might act as sintering additives for SiC) at ~ 1600 °C. Therefore, $Y_3Si_2C_2$ was also successfully used as a transition phase to achieve the seamless joining of SiC ceramics [7]. The joining mechanism was identified as follows: first, the laminated $Y_3Si_2C_2$ structure was formed by the *in situ* reaction between Y coatings with thickness of 500 nm and SiC matrix in the joining layer at a low temperature of 1400 °C, which subsequently disappeared owing to decomposition at high temperature of 1900 °C. More recently, high-entropy $RE_3Si_2C_2$ /rare earth oxides with strong electromagnetic wave absorption capability and wide efficient absorption bandwidth were proposed and successfully synthesized, which can undeniably broaden the applications potential of $RE_3Si_2C_2$ materials [8].

Even though the $Y_3Si_2C_2$ phase has been demonstrated as a promising sintering additive and joining material for SiC-based advanced ceramics, the synthesis method and basic properties (besides electrical and magnetic properties) of $Y_3Si_2C_2$ bulk ceramics have not been investigated. The only reported technique to synthesize $Y_3Si_2C_2$ bulk ceramics is the arc-melting of cold-pressed pellets of Y, Si, and C, and subsequent annealing in evacuated silica tubes for 30 days at 900 °C [1]. This process was found to be extremely time consuming, because Y ingots were used as raw materials and the reaction temperature was as low as 900 °C. Spark plasma sintering (SPS) is an effective consolidation ceramics technology, which enables densification of ceramics at relatively low sintering temperatures and short time compared to conventional methods, since the high-density electric current can promote mass diffusion [9, 10].

Therefore, the novel $Y_3Si_2C_2$ nano-laminated bulk ceramic material was successfully fabricated by the *in situ* reaction via SPS in this study. Furthermore, the phase composition, microstructure, mechanical properties, as well as electrical and thermal conductivity of $Y_3Si_2C_2$ were investigated. The measured Vickers hardness and elastic modulus were found to be in good agreement with the reported computational results.

2. Experimental

2.1. Preparation of $Y_3Si_2C_2$

YH_2 powder (Sinopharm Chemical Reagent Co., Ltd., Shanghai, China) with a purity of 99.5% and a mean particle size of 75 μm ; and β -SiC powder (99.5%, Eno Material Co., Ltd., Qinhuangdao, China) with a mean particle size of 0.5 μm , were used as raw materials. For the formation of $Y_3Si_2C_2$, the YH_2 and SiC powders were mixed in a stoichiometric ratio of 3.05:2. The *in situ* reaction sintering process was performed in an SPS furnace (HPD 25/1, FCT systems, Germany) under an Ar atmosphere at the temperature range of 1300–1500 °C for 30 min under a uniaxial pressure of 30 MPa. The heating and cooling rates were 50 °C min^{-1} . The as-obtained $Y_3Si_2C_2$ ceramics surfaces were polished using the final 1 μm diamond suspension.

2.2. Materials characterization

The phase compositions of the samples were identified by X-ray diffraction (XRD, D8 Advance, Bruker AXS, Germany) with CuK α radiation ($\lambda = 1.5406 \text{ \AA}$) under an operating voltage of 40 kV and current of 40 mA at a step scan of $0.02^\circ 2\theta$ and a step time of 0.2 s. The quantitative phase composition and lattice parameters of the Y₃Si₂C₂ phase were analyzed by Rietveld refinement by using the TOPAS software.

The surface and fracture micromorphology of the specimens were studied by scanning electron microscopy (SEM, Quanta 250 FEG, FEI, USA) system equipped with an energy dispersive spectroscopy (EDS) detector. The phase distributions and grain boundary map were characterized by electron back-scattered diffraction (EBSD) using a thermal field emission electron scanning microscope (Verios G4 uc, Thermo Scientific, USA) equipped with EBSD apparatus operating at 20 kV accelerating voltage. For the EBSD analysis, the samples were polished with the final 1 μm diamond suspension, followed by etching through an ion beam (BIB, TIC 3X, Leica, Germany) for 3 h [11]. The microstructure and phase compositions were investigated by transmission electron microscopy (TEM, Talos™ F200x, Thermo Fisher Scientific, USA) system equipped with EDS system. Thin foils for TEM observations were prepared by focused ion beam (FIB, Auriga, Carl Zeiss) technique.

2.3. Measurement of properties

Apparent density (ρ) of the samples was determined by the Archimedes' method. Elastic modulus was measured using a nanoindentation system (Hysitron PI85, Bruker) on the polished surface. Hardness of the materials was measured using a Vickers diamond indenter (HVs-1000 Digital micro Vickers Hardness Tester, Beijing Times Mountain Peak Technology Co., China) under a load of 0.5, 2, and 5 N, respectively, and a dwell time of 10 s. At least 20 indents were measured for each specimen. Electrical resistivity of samples was determined with a four-probe resistance tester (Cresbox, Napson Co., Japan). The thermal diffusivity coefficient (α) and specific heat capacity (C_p) were measured by laser flash method using a Netzsch LFA 457 apparatus (LFA, NETZSCH-Gerätebau GmbH, Germany). The thermal conductivity (κ , W m⁻¹ K⁻¹) was calculated by using Eq. (1) [12] as follows:

$$\kappa = \alpha\rho C_p \quad (1)$$

3. Results And Discussion

Figure 1 shows the XRD patterns of samples sintered at different temperatures. Y₃Si₂C₂ was the predominant phase for all the materials, while a trace amount of Y₂O₃ impurity phase was also detected. Rietveld refinement technique was applied to reveal the fundamental parameters. The amount of the predominant Y₃Si₂C₂ phase was 88.4, 94.3, and 94.5 wt.% for the samples sintered at 1300, 1400, and 1500 °C, respectively. The corresponding amount of the minor Y₂O₃ phase was 11.6, 5.7, and 5.5 wt.%, respectively. The lattice parameters of Y₃Si₂C₂ structure ($a = 8.4418 \text{ \AA}$, $b = 15.6671 \text{ \AA}$, and $c = 3.863 \text{ \AA}$) obtained from the Rietveld refinement are in good agreement with those determined by both the experimental measurements [2] and the calculation results [3], as presented in Table 1. The values of reliability factors for the refinement processing of the above mentioned three different samples were

found to be 9.1, 9.0, and 8.6%, respectively, which confirmed the reliability of the analysis and measurement approach.

Table 1
The experimental lattice parameters of $Y_3Si_2C_2$ derived from Rietveld refinement and SAED patterns, and their comparison with the calculated and experimental values reported in literature.

| $Y_3Si_2C_2$ | a (Å) | b (Å) | c (Å) | Ref. |
|-------------------|--------|---------|--------|------------|
| Experimental XRD | 8.4418 | 15.6671 | 3.863 | This study |
| Experimental SAED | 8.439 | 15.719 | / | This study |
| Calculated | 8.426 | 15.634 | 3.846 | [3] |
| Experimental | 8.4699 | 15.6971 | 3.8746 | [2] |

The formation of Y_2O_3 can be attributed to the presence of a trace amount of oxygen, introduced into the samples during mixing process or during sintering at high temperatures (as a trace impurity in Ar atmosphere). It is believed that YH_2 can react with SiC, thus the possible amount of residual Y decreases with increasing sintering temperature. As a result, the amount of Y_2O_3 impurity phase decreased from 11.6 to 5.7 wt.% when the sintering temperature was increased from 1300 to 1400 °C. The amount of Y_2O_3 at 1500 °C was only slightly lower than that detected for 1400 °C, which indicated that the reaction between YH_2 and SiC was almost complete at 1500 °C.

According to the actual phase compositions of the samples, the theoretical density was calculated by using the rule of mixture [13]. The theoretical density of $Y_3Si_2C_2$ (4.547 g cm^{-3}) and Y_2O_3 (5.02 g cm^{-3}) was used. The calculated theoretical density of the bulk samples was 4.596, 4.574, and 4.565 g cm^{-3} for the samples sintered at 1300, 1400, and 1500 °C, respectively. Thus, the relative density of as-obtained ceramics was 98.0% (1300 °C), 99.0% (1400 °C), and 99.5% (1500 °C), respectively. This clearly confirmed that high-purity and highly dense $Y_3Si_2C_2$ ceramic material was successfully obtained in a significantly shorter time compared to that reported in previous study, in which Y ingots were used [1]. Most probably, the use of Y-hydride raw powder instead of Y ingots facilitated the nucleation of $Y_3Si_2C_2$ [14]. At the same time, the use of pulsed current sintering improved the mass diffusion and promoted the solid state reaction to complete densification rapidly in a short period [15].

Figure 2 shows the microstructure of samples sintered at different temperatures, detected by EBSD. Figures 2a–c present the diffraction pattern quality quantified using the “band contrast”, while Figs. 2d–f show the phase distribution of $Y_3Si_2C_2$ (in red) and Y_2O_3 (in blue). The elongated, plate-like morphology of $Y_3Si_2C_2$ was clearly identified. The phase fraction of $Y_3Si_2C_2$ measured in the observed area increased with increasing sintering temperature: 80% (1300 °C), 84% (1400 °C), and 91% (1500 °C). At the same time, the grain size distribution is shown in Figs. 2g–i. The mean grain size of the materials increased

from 3.9 μm (1300 $^{\circ}\text{C}$) to 8.8 μm (1500 $^{\circ}\text{C}$). The abnormal grain growth was obviously observed when the sintering temperature was increased to 1400 and 1500 $^{\circ}\text{C}$.

Figures 3a–c show the fracture surfaces of $\text{Y}_3\text{Si}_2\text{C}_2$ sintered at 1300, 1400, and 1500 $^{\circ}\text{C}$, respectively. The failure mode was mainly intragranular, because of low shear deformation resistance of $\text{Y}_3\text{Si}_2\text{C}_2$ [3]. Some pores and a few un-reacted SiC fine grains (determined by EDS analysis, not shown here) were observed for the sample sintered at 1300 $^{\circ}\text{C}$ (Fig. 3a), while almost fully dense $\text{Y}_3\text{Si}_2\text{C}_2$ without any pores was observed after sintering at 1400 $^{\circ}\text{C}$ (Fig. 3b) and 1500 $^{\circ}\text{C}$ (Fig. 3c).

TEM analysis was carried out to observe the atomic-scale microstructure of the $\text{Y}_3\text{Si}_2\text{C}_2$ sintered at 1500 $^{\circ}\text{C}$. Figures 4a–e exhibit a high angle annular dark field (HAADF) image and the corresponding elemental distribution of Y, C, O, and Si, respectively. The semi-quantitative EDS analysis confirmed the presence of $\text{Y}_3\text{Si}_2\text{C}_2$ and Y_2O_3 , which correspond to the points 1 and 2 in Fig. 4a, respectively. The EDS results are presented in Table 2. The Y: Si ratio for the $\text{Y}_3\text{Si}_2\text{C}_2$ phase was measured to be around 1.8 by semi-quantitative EDS point analysis assuming that all oxygen was in the form of Y_2O_3 . The atomic-scale microstructure along the [001] zone axis was confirmed by HRTEM and corresponding SAED pattern shown in Figs. 4f and 4g. The layered atomic stacking can be clearly seen in the HRTEM image. The lattice fringe spacing of 0.786 nm can be assigned to the (020) planes of $\text{Y}_3\text{Si}_2\text{C}_2$, as shown in Fig. 4g. The corresponding SAED pattern also confirmed the orthorhombic crystal structure of $\text{Y}_3\text{Si}_2\text{C}_2$ (Fig. 4f). The lattice parameters were derived to be $a = 8.439 \text{ \AA}$ and $b = 15.719 \text{ \AA}$, which are in good agreement with those determined from the XRD pattern (Table 1).

Table 2
EDS results of the spots 1 and 2 in Fig. 3a.

| Spot number | Composition (at.%) | | | | Probable phase |
|-------------|--------------------|------|------|------|-----------------------------------|
| | Y | Si | C | O | |
| 1 | 48.3 | 23.2 | 19.7 | 8.8 | $\text{Y}_3\text{Si}_2\text{C}_2$ |
| 2 | 42.2 | 0 | 4.5 | 53.3 | Y_2O_3 |

The properties of $\text{Y}_3\text{Si}_2\text{C}_2$ and some typical ternary carbides are listed in Table 3. The elastic modulus and Vickers hardness of the materials decreased with increasing sintering temperature. This was probably caused by a decreasing amount of Y_2O_3 in the materials with increasing temperature. The elastic modulus and Vickers hardness of Y_2O_3 are ~ 180 and 7.6 GPa [19–21], respectively, which are slightly higher than the calculated values for $\text{Y}_3\text{Si}_2\text{C}_2$ [3]. Moreover, the grain size increased with increasing sintering temperature, thus the Vickers hardness also decreased with the increase in the sintering temperature according to the Hall–Petch relationship. The elastic modulus of the sample sintered at 1500 $^{\circ}\text{C}$ was close to the calculated values reported by Zhou et al. [3]. The Vickers hardness of

the sample sintered at 1500 °C was 7.2 ± 0.8 , 6.5 ± 0.5 , and 6.4 ± 0.4 GPa for the indentation load of 0.5, 2, and 5 N, respectively. These values are in good agreement with the reported calculated value of 6.9 GPa [3].

Table 3

Density, mechanical, thermal and electrical properties of the as-obtained $Y_3Si_2C_2$ and their comparison with the reported values of typical ternary layered structural ceramics

| Properties | $Y_3Si_2C_2$ | | | Theoretical [1, 3] | YAl_3C_3 [16] | Ti_3SiC_2 [17] | Ti_3AlC_2 [18] |
|--|--------------|---------|---------|-----------------------|--------------------|---------------------|---------------------|
| | 1300 °C | 1400 °C | 1500 °C | | | | |
| Theoretical density (g/cm ³) | 4.504 | 4.528 | 4.543 | 4.547 | 3.90 | 4.52 | 4.2 |
| Elastic modulus (GPa) | 185 | 177 | 156 | 127 | 325 | 322 | 297 |
| Vickers hardness (GPa)* | 6.9 | 6.7 | 6.4 | 6.9 | 12.6 | 4 | 3.5 |
| Thermal conductivity (W m ⁻¹ k ⁻¹) | 16.1 | 15.7 | 13.7 | N/A | N/A | 37 | 40 |
| Electrical resistivity (10 ⁻⁶ Ω•cm) | 132.2 | 138.2 | 159.1 | 100–270 | N/A | 22.7 | 38.7 |

* The value of the Vickers hardness was measured with the load of 5N.

The shape of Vickers indents was irregular with the exfoliated surfaces and deformed particles, which is similar to the typical indent shape of Ti_3SiC_2 MAX phase [22]. A typical surface morphology at the tip of a Vickers indent for the $Y_3Si_2C_2$ sample sintered at 1500 °C is shown in Figs. 5a and 5b. Interestingly, in the case of basal $Y_3Si_2C_2$ plane oriented parallel to the indentation load, typical nano-laminated fracture was observed, owing to the kink boundaries, delamination, and slipping (Fig. 5a). Such behavior is commonly observed for the group of MAX phases, which belong to typical damage tolerant ceramics [23]. On the other hand, when the basal plane of $Y_3Si_2C_2$ was oriented in a direction perpendicular to the indentation load, the exfoliation and sharp steps-like fracture caused by crack deflection inside the $Y_3Si_2C_2$ grains was observed (Fig. 5b). The fracture energy can be consumed by virtue of crack deflection. A typical nano-laminated MAX phase-like structure of $Y_3Si_2C_2$ is shown in Fig. 5c, which can be easily recognized by its cleavage nature. The low Vickers hardness and typical nano-laminated fracture behavior indicated that $Y_3Si_2C_2$ belongs to the group of soft ceramics. Zhou et al. reported that the low shear deformation

resistance along the (010) [101] slip system could be attributed to the weak metallic bonding between Y_2-C [3].

Thermal conductivity of samples decreased from 16.1 to 13.7 $W m^{-1} k^{-1}$ with the increase in the sintering temperature from 1300 to 1500 °C. This was observed despite the fact that the grain size increased with increasing sintering temperature (Fig. 2), which usually leads to the improved thermal conductivity due to the decreased phonon scattering by the grain boundaries. Therefore, the decreased thermal conductivity with increasing sintering temperature in this study can be attributed to the content of high thermal conductivity phase - Y_2O_3 ($27 W m^{-1} k^{-1}$) [24], which also decreased with increasing temperature.

The electrical resistivity of the samples is presented in Table 3. The corresponding electrical conductivity of samples sintered at 1300, 1400, and 1500 °C was calculated to be 7.6×10^5 , 7.6×10^5 , and $6.3 \times 10^5 S m^{-1}$, respectively. The main contribution to the electrical conductivity of $Y_3Si_2C_2$ was mainly from $Y1 4d_{eg}$, $Y2 4d_{2g}$, $C 2p_{x'}$, and $C 2p_{z'}$ states (x' and z' are inclined to the x and z axis, respectively, at about 45°) based on the analysis of the projected density of states and the decomposed distribution of electron density [3].

4. Conclusions

The high-purity highly dense $Y_3Si_2C_2$ ceramic material, for the first time, was fabricated by *in situ* solid state reaction between YH_2 and SiC via SPS. The as-obtained $Y_3Si_2C_2$ ceramic exhibited a nano-laminated structure, which was confirmed by HRTEM analysis. The lattice parameters were derived as $a = 8.4418 \text{ \AA}$, $b = 15.6671 \text{ \AA}$, and $c = 3.863 \text{ \AA}$ by the Rietveld refinement of XRD patterns. The experimentally measured elastic modulus (156 GPa) and Vickers hardness (6.4 GPa) of the fabricated ceramics are in good agreement with the reported theoretically calculated values. Typical nano-laminated fracture behavior was observed at the tip of Vickers indents, which indicated that $Y_3Si_2C_2$ belongs to the group of soft ceramics. The thermal and electrical conductivity of the sample sintered at 1500 °C was $13.7 W m^{-1} k^{-1}$ and $6.3 \times 10^5 S m^{-1}$, respectively. The proposed synthesized strategy could potentially be used to fabricate other $RE_3Si_2C_2$ phases.

Declarations

Acknowledgments

We would like to recognize the support from the Ningbo 3315 Innovative Teams Program, China (Grant NO. 2019A-14-C). This study was supported by the National Natural Science Foundation of China (Grant No. 11975296 and 51811540402).

References

- [1] Gerdes MH, Witte AM, Jeitschko W, et al. Magnetic and Electrical Properties of a New Series of Rare Earth Silicide Carbides with the Composition $R_3Si_2C_2$ (R = Y, La–Nd, Sm, Gd–Tm). *J Solid State Chem.* 1998, 138: 201-206.
- [2] Jeitschko W, Gerdes MH, Witte AM, et al. Subcell Structure and Two Different Superstructures of the Rare Earth Metal Silicide Carbides $Y_3Si_2C_2$, $Pr_3Si_2C_2$, $Tb_3Si_2C_2$, and $Dy_3Si_2C_2$. *J. Solid State Chem* 2001, 156 :1-9.
- [3] Zhou YC, Xiang HM, Dai FZ, Y_5Si_3C and $Y_3Si_2C_2$: Theoretically predicted MAX phase like damage tolerant ceramics and promising interphase materials for SiC_f/SiC composites. *J Mater Sci Technol* 2019, 35: 313-322.
- [4] Xu K, Zou H, Chang K, et al. Thermodynamic description of the sintering aid system in silicon carbide ceramics with the addition of yttrium. *J Eur Ceram Soc* 39 2019, 15: 4510-4519.
- [5] Shao JQ, Li M, Chang KK, et al. Fabrication and characterization of SPS sintered SiC-based ceramic from $Y_3Si_2C_2$ -coated SiC powders. *J Eur Ceram Soc* 2018, 38: 4833-4841.
- [6] Liu JW, Zhou XB, Tatarko P, et al. Fabrication, microstructure, and properties of SiC/Al_4SiC_4 multiphase ceramics via an in-situ formed liquid phase sintering. *J Adv Ceram* 2020, 9: 193-203.
- [7] Zhou XB, Liu JW, Zou SR, et al. Almost Seamless Joining of SiC Using an In-situ Reaction Transition Phase of $Y_3Si_2C_2$. *J Eur Ceram Soc* 2020, 40: 259-266.
- [8] Chen H, Zhao B, Zhao ZF, et al. Achieving strong microwave absorption capability and wide absorption bandwidth through a combination of high entropy rare earth silicide carbides/rare earth oxides. *J Mater Sci Technol* 2020, 47: 216-222.
- [9] Hrubovčáková M, Múdra E, Bureš R, et al. Microstructure, fracture behaviour and mechanical properties of conductive alumina based composites manufactured by SPS from graphenated Al_2O_3 . *J Eur Ceram Soc* 2020, 40: 4818-4824.
- [10] Marzieh E, Mohammad Z, Mansour R. The effect of temperature on the physical and mechanical properties of nanostructured boron nitride by spark plasma sintering. *J Alloys Compds* 2020, 835:
- [11] Jiang RR, Li M, Yao YR, et al. Application of BIB polishing technology in cross-section preparation of porous, layered and powder materials: A review, *Front. Mater Sci* 2019, 13: 107-125
- [12] Volz E, Roosen A, Hartung W, Winnacker A. Electrical and thermal conductivity of liquid phase sintered SiC. *J Eur Ceram Soc* 2001, 21: 2089-2093.
- [13] Zou J, Zhang GJ, Fu ZY. In-situ ZrB_2 -hBN ceramics with high strength and low elasticity. *J Mater Sci Technol* 2020, 48: 186-193.

- [14] Lapauw T, Halim J, Lu J, et al. Synthesis of the novel Zr_3AlC_2 MAX phase. *J Eur Ceram Soc* 2016, 36: 943-947.
- [15] Munirw ZA, Quach DV, Ohyanagi M, Electric Current Activation of Sintering: A Review of the Pulsed Electric Current Sintering Process. *J Am Ceram Soc* 2011, 94: 1-19.
- [16] Zhao GR, Chen JX, Li YM, et al. In situ synthesis, structure, and properties of bulk nanolaminate YAl_3C_3 ceramic. *J Eur Ceram Soc* 2017, 37: 83-89.
- [17] Barsoum MW, The $M_{N+1}AX_N$ phases: a new class of solids: Thermodynamically Stable Nanolaminates. *Prog Solid State Chem* 2000, 28: 201-281.
- [18] Tzenov NV, Barsoum MW, Synthesis and characterization of Ti_3AlC_2 . *J Am Ceram Soc* 2000, 83: 825-832.
- [19] Zhang L, Feng J, Pan W. Vacuum sintering of transparent $Cr:Y_2O_3$ ceramics. *Ceram Inter* 2015, 41: 8755-8760.
- [20] Ahmadi B, Reza SR, Ahsanzadeh-Vadeqani M, et al. Mechanical and optical properties of spark plasma sintered transparent Y_2O_3 ceramics. *Ceram Inter* 2016, 42: 17081-17088.
- [21] Yeheskel O, Tevet O. Elastic moduli of transparent yttria. *J Am Ceram Soc* 1999, 82: 136-144.
- [22] Zhou XB, Jing L, Kwon YD, et al. Fabrication of SiC_w/Ti_3SiC_2 composites with improved thermal conductivity and mechanical properties using spark plasma sintering. *J Adv Ceram* 2020, 9: 462-470.
- [23] Tatarko P, Chlup Z, Mahajan A, et al. High temperature properties of the monolithic CVD β -SiC materials joined with a pre-sintered MAX phase Ti_3SiC_2 interlayer via solid-state diffusion bonding. *J Eur Ceram Soc* 2017, 37: 1205-1216.
- [24] Yi Q, Zhou SM, Teng H, et al. Structural and optical properties of $Tm:Y_2O_3$ transparent ceramic with La_2O_3 , ZrO_2 as composite sintering aid. *J Eur Ceram Soc* 2012, 32: 381-388.

Figures

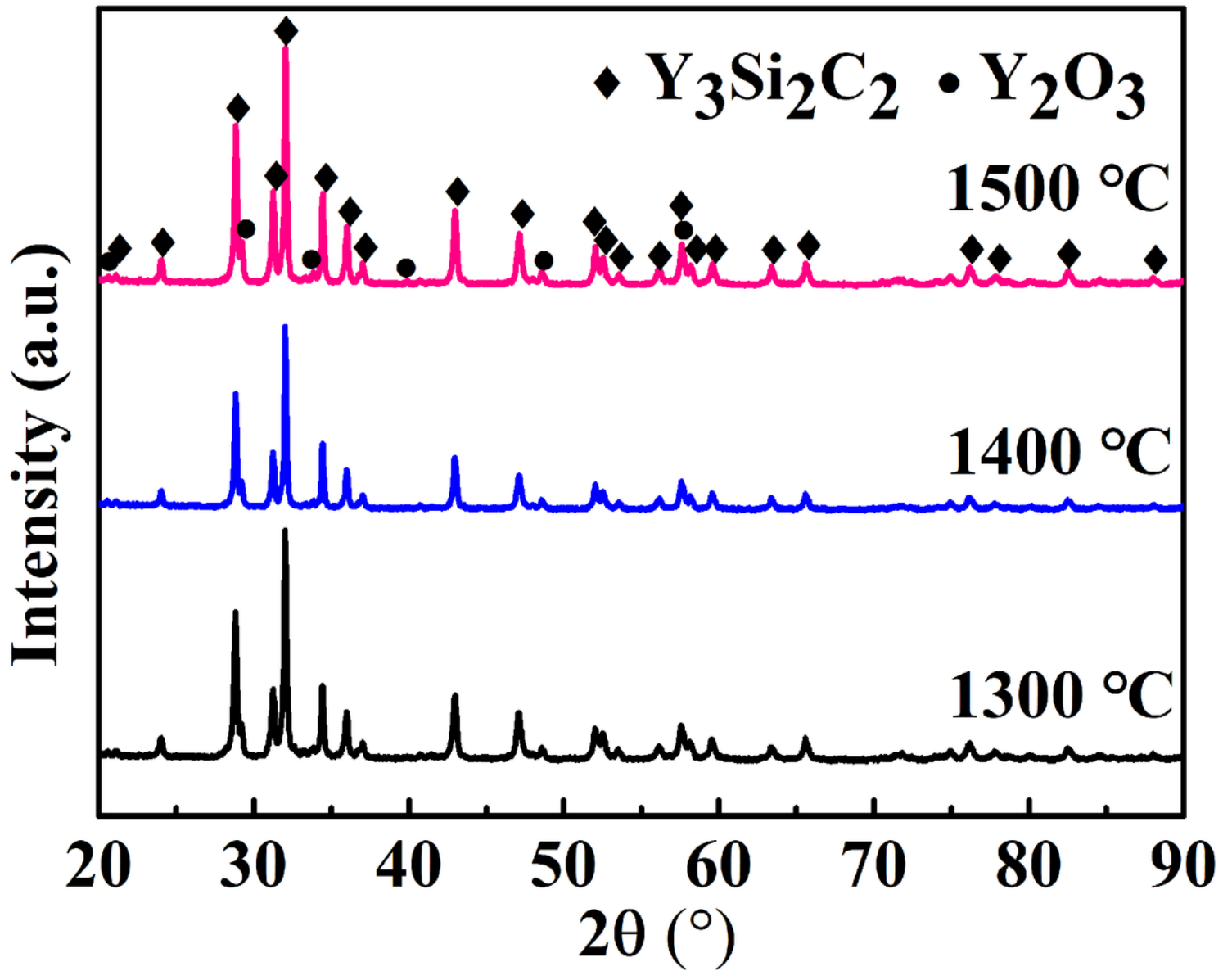


Figure 1

XRD patterns of $\text{Y}_3\text{Si}_2\text{C}_2$ sintered at various temperatures by reactive SPS.

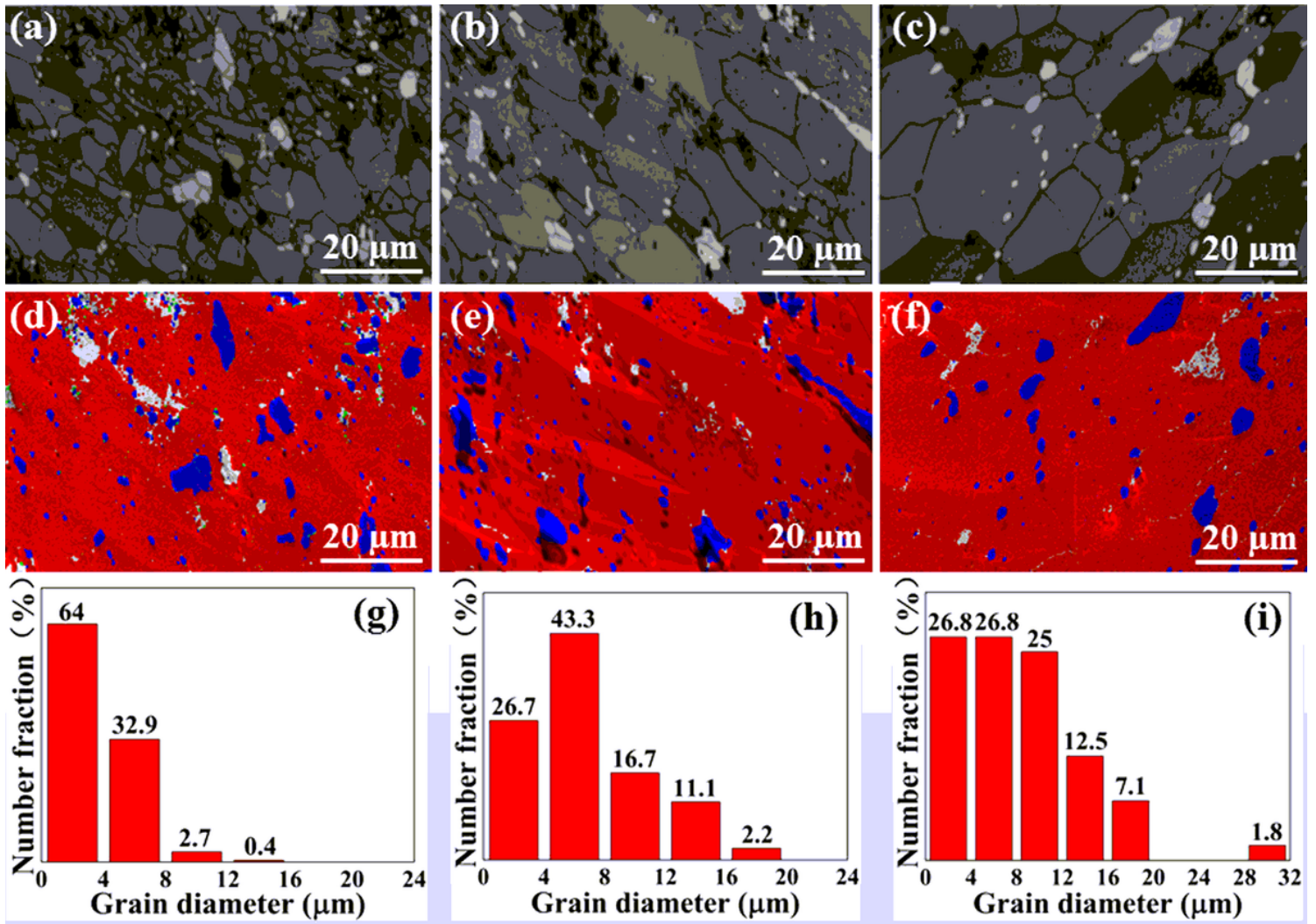


Figure 2

Microstructure of samples fabricated at various temperatures observed by EBSD: micrograph in band contrast (a) 1300 °C; (b) 1400 °C; (c) 1500 °C; phase distribution: Y₃Si₂C₂ in red and Y₂O₃ in blue (d) 1300 °C; (e) 1400 °C; (f) 1500 °C; grain size distribution (g) 1300 °C; (h) 1400 °C; (i) 1500 °C.

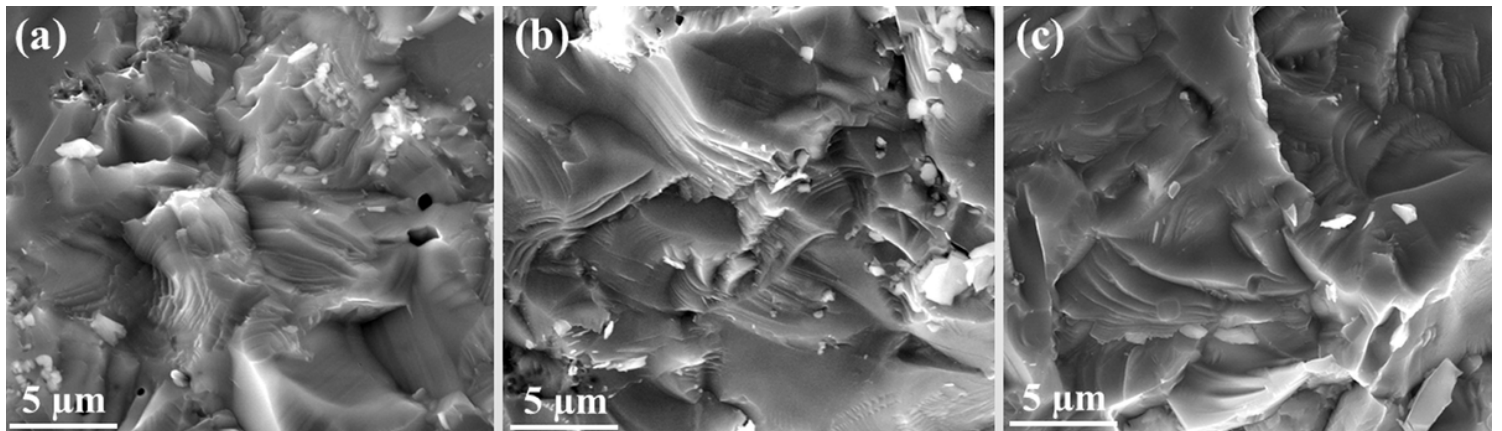


Figure 3

SEM images of the fractured surfaces of Y₃Si₂C₂ sintered by reactive SPS at (a) 1300 °C; (b) 1400 °C; (c) 1500 °C.

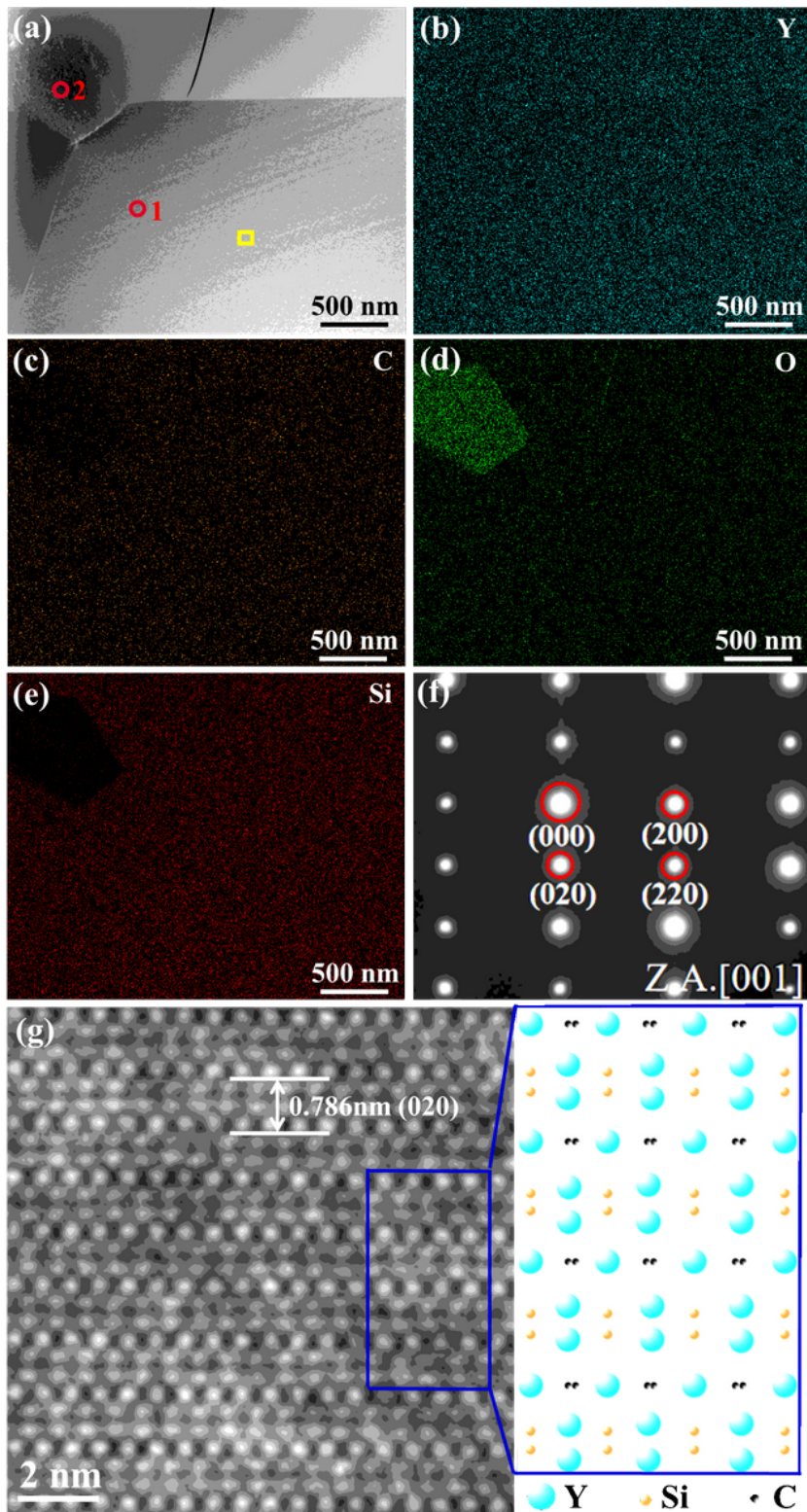


Figure 4

TEM image of Y₃Si₂C₂ ceramics sintered at 1500 °C: (a) HAADF image and elemental distribution of (b) Y; (c) C; (d) O; (e) Si; (f) SAED pattern for the yellow area in (a); (g) HRTEM image of Y₃Si₂C₂, the insert includes structure models showing the positions of Y, Si, and C.

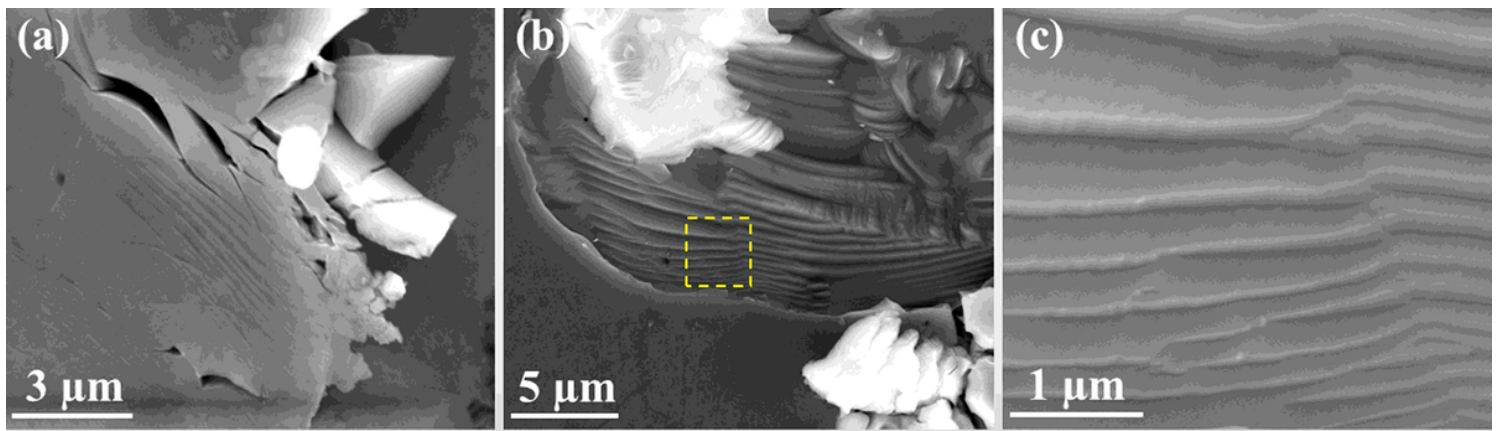


Figure 5

Surface morphology of sample sintered at $1500\ ^\circ C$ after Vickers indentation test: (a) basal $Y_3Si_2C_2$ plane oriented parallel to the load with the presence of kinks, delamination, and slipping; (b) basal $Y_3Si_2C_2$ plane oriented perpendicular to the load showing the exfoliation; (c) high magnification SEM image showing the nano-laminated structure of $Y_3Si_2C_2$.